Influence of aluminum doping on the properties of $LiCoO_2$ and $LiNi_{0.5}Co_{0.5}O_2$ oxides

S Castro-García [a], A Castro-Couceiro[a], M.A Señarís-Rodríguez[a], F Soulette[b], C Julien[b]

a Departamento de Química Fundamental, Facultad de Ciencias, Universidad de A Coruña, A Zapateira, 15071 A Coruña, Spain

b LMDH, UMR 7603, Université Pierre et Marie Curie, 4 place Jussieu, 75252 Paris cedex 05, France

Solid State Ionics

Volume 156, Issues 1–2, January 2003, Pages 15–26

Received 25 March 2002, Revised 17 June 2002, Accepted 18 June 2002, Available online 3 December 2002

doi:10.1016/S0167-2738(02)00570-2

Abstract

We have prepared $LiCo_{1-y}Al_yO_2$ and $LiNi_{0.5-y}Al_yCo_{0.5}O_2$ ($0 \le y \le 0.3$) powder samples by a low temperature sol–gel method using succinic acid as chelating agent. We have studied the details of their crystallographic and local structure by X-ray diffraction (XRD) and FTIR spectroscopy, respectively; we have analyzed their chemical composition by ICP and obtained information about the morphology of the polycrystalline particles by SEM. Also, we have studied the electrochemical performance of the as-prepared materials in the $Li/LiNi_{0.5-y}Al_yCo_{0.5}O_2$ cells cycled in the potential range 2.5–4.2 V finding that the overall capacity of the oxides has been reduced due to the metal substitution. For example, at 4.2 V cut-off, the charge capacity of the $Li/LiNi_{0.35}Al_{0.15}Co_{0.5}O_2$ cell is ca. 115 mA h/g. However, more stable

charge–discharge cycling performances have been obtained as compared to those displayed by the native oxides. Finally, we have characterized the kinetics of Li-diffusion by the galvanostatic intermittent titration technique and, according to our results, Al substitution provides an increase in the chemical diffusion coefficients of Li ions in the $LiNi_{0.5-y}Al_yCo_{0.5}O_2$ matrix.

Keywords

Lithium battery; Sol–gel synthesis; Cathode material; Lithium cobalt oxide; Lithium nickel oxide; Lithium aluminum cobalt oxide

Keywords

$LiCo_{1-y}Al_yO_2$; $LiNi_{0.5-y}Al_yCo_{0.5}O_2$

1. Introduction

Ten years ago, commercial lithium-ion batteries were introduced on the market to power portable electronics used as cellular telephones, video tape recorders, laptop computers, etc. $LiCoO_2$ is the most studied cathode for these rechargeable lithium-ion batteries. Its layered α-$NaFeO_2$ type structure ($R\bar{3}m$ space group) provides structural flexibility to introduce Li ion as mobile guest species. This oxide is considered to have high specific density, high voltage, long cycle life and remarkable reversibility for lithium intercalation–deintercalation process. It is easy to prepare but its high cost and toxicity remain problems to be solved [1].

Looking for lower cost substituted, other isostructural lithium mixed oxides have been considered, among them $LiNiO_2$. This compound has the advantage of presenting a higher specific capacity for lithium cycling; nevertheless, it is difficult to prepare in the layered structure due to the tendency of lithium and nickel to disorder, leading to a deterioration of their electrochemical performance. However, the layered structure can be stabilized in mixed Co/Ni compounds $LiCo_{1-y}Ni_yO_2$, for nickel contents up to $y \leq 0.8$, resulting in improvements in the cycling life and rate of the electrodes [2] and [3].

Apart form nickel substituted compounds, intensive investigations have been also carried out on other doped $LiCo_{1-y}M_yO_2$ oxides (M=Mn, Cr, Al, Ti, B, Mg, etc.), which

show interesting structural and electrochemical properties [4], [5], [6], [7], [8], [9], [10], [11], [12] and [13].

Doping with non-transition metals as aluminum has gained in interest for several reasons:

- the low cost, low toxicity and low density of aluminum;
- the isostructurality of α-$LiAlO_2$ with $LiCoO_2$ and the similarity in the ionic radii of Al^{3+} and Co^{3+}($^{VI}r_{Al}{}^{3+}$=0.535 Å; $^{VI}r_{Co}{}^{3+}{}_{(l.s.)}$=0.545 Å [14]), which allows a wide range of solid solution $LiCo_{1-y}Al_yO_2$[15], [16], [17] and [18];
- the fact that aluminum substitution for transition metal oxides leads to higher lithium intercalation voltages, as predicted and verified experimentally by Ceder et al. [18] and [19];
- the stabilizing effect of this doping on the layered structure, which extends the cyclability and enhances the capacity of the electrochemical cells [18], [20], [21] and [22].

Despite all these advantages, it has been found that Al-doped $LiCoO_2$ electrodes show large capacity fading during cycling [18] and [19], which are probably related to structural defects of cathode materials[15].

On the other hand, it is known that the electrochemical performance of these polycrystalline oxides is largely governed by the chemical stoichiometry, homogeneity, crystallinity and size of the particles. Solid-state reactions, which are the traditional method used for obtaining these lithiated mixed oxides, have several drawbacks, among them that of not allowing the control of the morphology of the final products. Meanwhile, wet-chemistry methods that provide a better mixing of the reagents and a better reactivity of the mixture (resulting in lower heating treatments and shorter reaction times) allow a better control over the morphology, homogeneity and microstructural properties of the materials [23].

In this study, we have prepared $LiCo_{1-y}Al_yO_2$ and $LiNi_{0.5-y}Al_yCo_{0.5}O_2$ samples using a solution method based on a typical sol–gel reaction, using succinic acid as chelating agent. Here we present the results of our studies about the solid solubility of aluminum in both the $LiCoO_2$ oxide and in the mixed cobalt–nickel compound $LiNi_{0.5}Co_{0.5}O_2$, and the effect of the aluminum doping on the structural, compositional and electrochemical properties of the resulting materials.

2. Experimental

The $LiCo_{1-y}Al_yO_2$ and $LiNi_{0.5-y}Al_yCo_{0.5}O_2$ ($0 \le y \le 0.3$) samples were prepared by a sol–gel method using succinic acid ($C_4H_6O_4$) as chelating agent. To prepare 1 g of final product, we have dissolved the stoichiometric amounts of metal salts (pure reagents (>99%) $LiCH_3CO_2 \cdot 2H_2O$, $Co(CH_3CO_2)_2 \cdot 4H_2O$, $Ni(CH_3CO_2)_2 \cdot 4H_2O$ and $Al(NO_3)_3 \cdot 9H_2O$) in approximately 50 ml of distilled water to obtain clear solutions. Succinic acid (in a total acid/metals molar ratio of 0.5) was added and then the resulting solutions were mixed with a magnetic stirrer at 80 °C to obtain homogeneous viscous gels. The gels were heated at 100–200 °C for less than 2 h to get the precursor powders. These precursors were decomposed at 400 °C in air in order to eliminate the organic residues. Finally, the materials were successively calcined at 700 °C during 2 h in air and at 800 °C during 4 h in oxygen.

The thermal decomposition behavior of the gels was examined by means of thermogravimetry (TG/DTA) using a STD-2960 T.A. Instruments analyzer. Measurements were carried out in the temperature range of $25 \le T \le 1100$ °C under a flow of dry air, and using a heating rate of 10 °C/min. Elemental analysis of the final products was carried out using a VG PlasmaQuad II-S induced-coupled-plasma (ICP) mass-spectrometer after dissolving the given powder samples in HCl. X-ray powder diffraction patterns were recorded with a D-5000 Siemens X-ray diffractometer, using nickel-filtered CuKα radiation (λ=1.5406 Å). The XRD data were analyzed by the Rietveld profile analysis using the RIETICA program [24]. The morphology of the samples was studied by scanning electron microscopy (SEM) using a JSM-6400 JEOL microscope. Infrared absorption spectra were recorded at room temperature using a Fourier-transform interferometer (model Bruker IFS113v). In the 100–700 cm^{-1} spectral range, this vacuum bench apparatus was equipped with a 3.5-μm-thick Mylar beamsplitter, a global source, and a DTGS/PE far-infrared detector. IR data were collected in transmission mode at a spectral resolution of 2 cm^{-1} after 256 scans in vacuum atmosphere. For these studies, the samples were ground to fine powders and dispersed in ICs pellets.

The electrochemical studies were carried out using laboratory-scale Li□$LiNi_{0.5-y}Al_yCo_{0.5}O_2$ cells that were fabricated employing a nonaqueous electrolyte (1 M $LiPF_6$ in (1:1) EC–DMC mixture). The typical composite positive electrodes consisted of the mixture of active $LiNi_{0.5-y}Al_yCo_{0.5}O_2$ powders, acetylene black and colloidal PTFE binder in the 90:5:5 weight ratios. This mixture was pressed onto an expanded aluminum microgrid at a pressure of 500 MPa, resulting in a circular pellet electrode

whose diameter was 10 mm. The pellets were then dried at 120 °C in air. Glass paper membrane was used as the separator between the positive electrode and the lithium metal foil used as negative electrode. Electrodes and separators were housed in a Teflon laboratory cell. Galvanostatic charge–discharge cycles were recorded using a Mac-Pile system at a slow scan mode (i.e. current pulse of 0.1 mA/cm^2 for 1 h followed by a relaxation period of 0.5 h) in the potential range 2.5–4.2 V. The chemical diffusion coefficients of Li^+ ions (D_{Li^+}) in $LiNi_{0.5-y}Al_yCo_{0.5}O_2$ electrode materials were measured using the galvanostatic intermittent titration technique (GITT) [25]. In this method, the transient voltage generated by applied current pulse (I_o) is measured as a function of time and decays as the Li^+ ions diffuse throughout the host lattice.

3. Results and discussion

3.1. Thermal stability (TGA/DTA)

We performed thermogravimetric and differential thermal analysis of the precursor gels dried at ~200 °C to study the thermal stability of the samples and to optimize the calcination temperatures for the gel precursors. We show some representative results in Fig. 1, Fig. 2 and Fig. 3. The loss of weight at temperatures T<200 °C indicates water elimination. The main weight loss, which is observed in the temperature range 200–700 °C and gives rise to an exothermic peak centered at 250 °C in the DTA curve(Fig. 3), corresponds to the gel decomposition. It leads to well-crystallized $LiCo_{1-y}Al_yO_2$ (Fig. 1) and $LiNi_{0.5-y}Al_yCo_{0.5}O_2$ (Fig. 2) oxides at temperatures that are lower than those required in solid-state reactions. This is an important result because high calcination temperatures promote the growth of the grains, and moreover, they induce lithium deficiency in the final products.

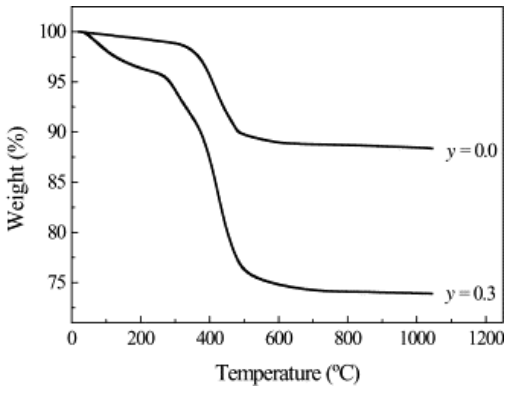

Fig. 1.
TGA curves of $LiCo_{1-y}Al_yO_2$ dried-gel precursors.

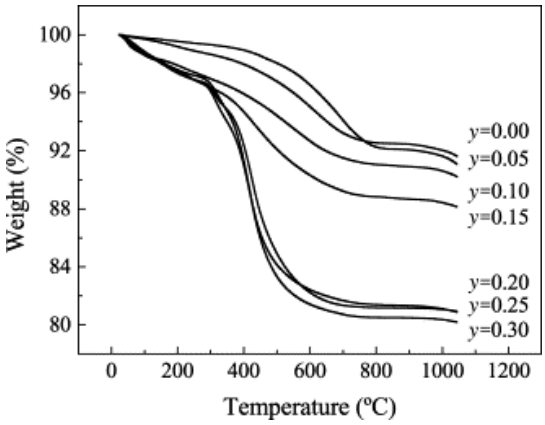

Fig. 2.
TGA curves of $LiNi_{0.5-y}Al_yCo_{0.5}O_2$ dried-gel precursors.

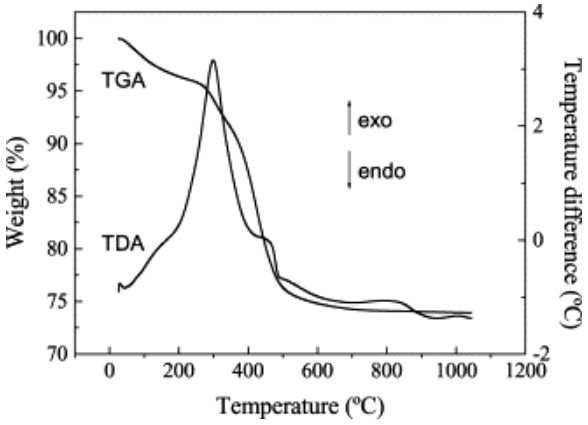

Fig. 3.
TGA and DTA curves of $LiCo_{0.7}Al_{0.3}O_2$ dried-gel precursor.

As it has been previously observed in the Al-free compounds $LiCoO_2$, $LiNiO_2$[26], the presence of Ni in these samples stabilizes the gel probably due to a strong Ni coordination to the donor atoms and delays its decomposition, which takes place at higher temperatures. Similarly, in the case of the Al-doped compounds, it is observed that the Li–Co–Al precursor gels decompose almost completely at 600 °C (Fig. 1) (as it occurs in Al-free Li–Co precursor gels), while in the case of the Li–Ni–Al–Co precursors, the higher the Ni content, the higher the decomposition temperature. Lastly, as it can be seen in Fig. 2, while the samples $LiNi_{0.5-y}Al_yCo_{0.5}O_2$ with $y \leq 0.15$ decompose at 800 °C, in the samples with $y \geq 0.20$ the main weight loss ends at a lower temperature (around 600 °C).

On the other hand, at higher temperatures (above 1000 °C in all the Li–Co–Al samples and in the highly doped Li–Ni–Al–Co samples ($y \geq 0.20$) and above ~900 °C in the low-doped Li–Ni–Al–Co samples ($y < 0.20$)), a small weight loss is also observed, that it is attributed to the departure of lithium oxide from the framework. It is also well known that a high nickel content favors the loss of lithium in these lamellar oxides because of its tendency to form the non-stoichiometric phase that contains Ni^{2+} ions in the lithium sites of the α-$NaFeO_2$ structure [27]. Thus, we can conclude that aluminum substitution

for nickel reduces the tendency to lithium loss and improves the thermal stability in these samples.

3.2. X-ray powder diffraction results (XRD)

The crystal chemistry of these Al-doped samples was carefully investigated by XRD studies. As a general example for the two series, Fig. 4 shows the XRD patterns of one of the gel-derived samples ($LiNi_{0.35}Al_{0.15}Co_{0.5}O_2$) treated at various temperatures. In all cases, the materials are single phase from the lowest temperature and all diffraction lines can be indexed assuming a hexagonal (hex) lattice, which corresponds to the quasi-layered α-$NaFeO_2$ type structure (space group $R\bar{3}m$). This structure belongs to the rhombohedral system in which Li^+, M^{3+} (M=Co, Ni, Al) and O^{2-} occupy 3a, 3b and 6c sites (Wyckoff notations), respectively. As the heating temperature gets higher, the diffraction peaks get sharper and the width of the peaks narrower due to an increase in the samples crystallinity and a gradual growth of the average particle size.

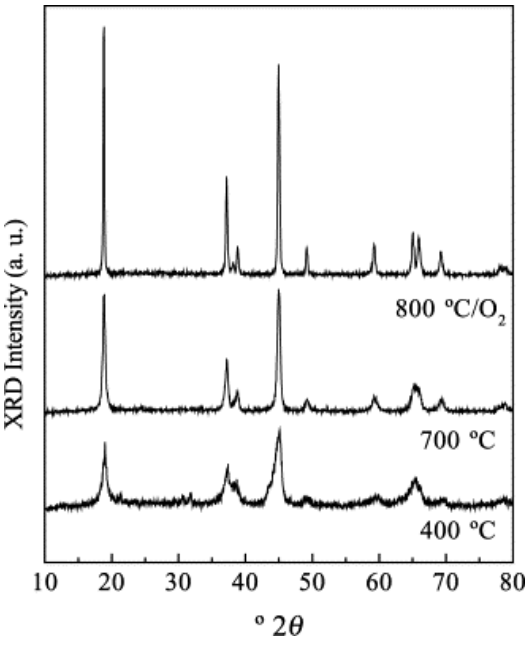

Fig. 4.
XRD patterns for the $LiNi_{0.35}Al_{0.15}Co_{0.5}O_2$ gel-derived powders calcined in O_2 atmosphere at various temperatures in the range 400–800 °C.

The XRD patterns of the powders treated at 800 °C (Fig. 5a and b) show a (003)/(104) ratio intensity >1 and well-defined (006)–(102) and (108)–(110) doublets. These results are a primary indication of an ordered distribution of Li and Co/Ni/Al in the layered structure [28] and [29].

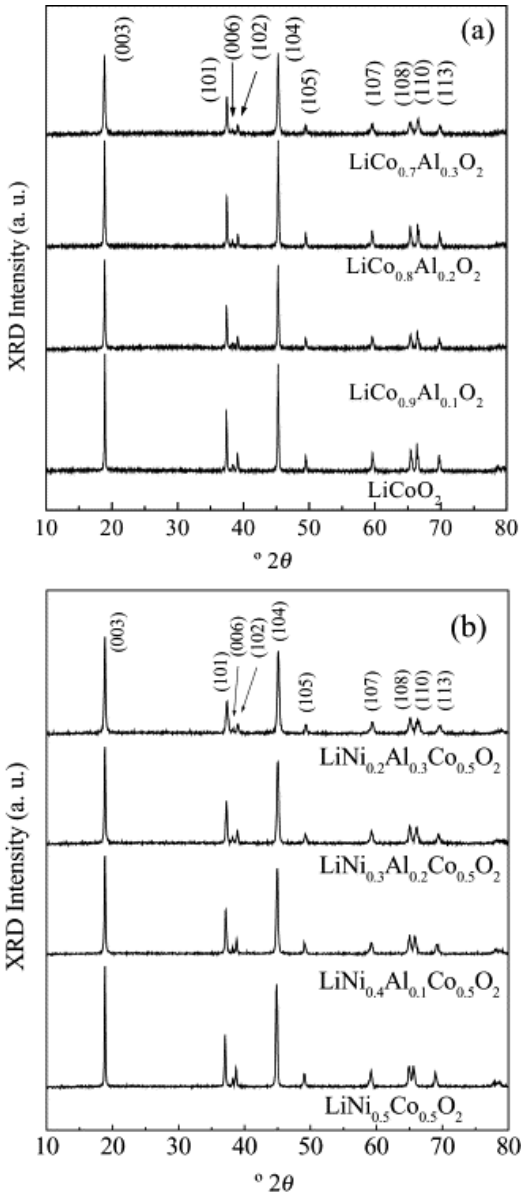

Fig. 5.
XRD patterns for (a) $LiCo_{1-y}Al_yO_2$ and (b) $LiNi_{0.5-y}Al_yCo_{0.5}O_2$ powders calcined at 800 °C.

The lattice parameters obtained by Rietveld refinements show significant changes upon Al substitution (Fig. 6a and b; Table 1 and Table 2) revealing that the major phase is a solid solution containing increasing amounts of the dopant. In this context, the a_{hex} cell parameter decreases with *y* due to the incorporation of the smaller and more polarizing Al^{+3} ion ($^{VI}r_{Al}{}^{3+}$=0.535 Å) in place of the larger Co^{+3} ($^{VI}r_{Co}{}^{3+}{}_{(l.s.)}$=0.545 Å) or Ni^{+3} ($^{VI}r_{Ni}{}^{3+}{}_{(l.s.)}$=0.69 Å) ions [14], depending on the series. As it was expected, the decrease of the a_{hex}parameter is more important when aluminum substitutes for nickel than for cobalt. On the other hand, thec_{hex} parameter is seen to increase slightly upon doping, even if the rise is smaller in the Li–Ni–Al–Co series. This result can be understood on the basis of the two competing and opposite effects that this doping produces on the structure: (a) the polarizing effect of the Al^{3+} ion in the $[MO_2]$ layers will tend to distort the structure and increase the interlayer distance along *c*-axis; (b) the reduction in the size of the cation will tend to shrink the structure, specially in the case

of the substitution of the smaller cation Al^{3+} for the largest cation Ni^{3+}. As these two factors will be more balanced in the case of the Li–Ni–Al–Co series, the variation of c_{hex} will be more limited in those materials. These XRD data are consistent with the earlier reported by Yoon et al. [17] and by Jang et al. [18].

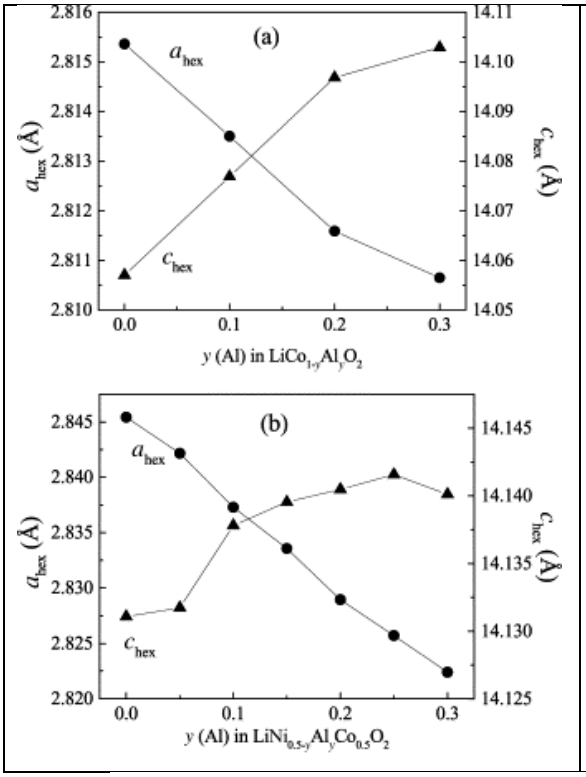

Fig. 6.
Variation of lattice constants as a function of aluminum content in (a) $LiCo_{1-y}Al_yO_2$ and (b) $LiNi_{0.5-y}Al_yCo_{0.5}O_2$, obtained by Rietveld refinements.

Table 1.
Rietveld refinement results for $LiCo_{1-y}Al_yO_2$ ($0 \le y \le 0.3$)

Sample	a_{hex} (Å)	c_{hex} (Å)	c_{hex}/a_{hex}	V_{hex} (Å^3)	R_{wp}	R_B
$LiCoO_2$	2.81534(3)	14.0564(2)	4.9928	96.486(2)	12.99	5.43
$LiCo_{0.9}Al_{0.1}O_2$	2.81422(5)	14.0659(4)	4.9982	96.475(4)	12.61	4.07
$LiCo_{0.8}Al_{0.2}O_2$	2.81190(6)	14.0945(6)	5.0124	96.511(5)	12.27	3.56
$LiCo_{0.7}Al_{0.3}O_2$	2.81083(7)	14.0991(7)	5.0160	96.469(6)	12.76	3.73

Table 2.

Rietveld refinement results for $LiNi_{0.5-y}Al_yCo_{0.5}O_2$ ($0 \leq y \leq 0.3$)

Sample	a_{hex} (Å)	c_{hex} (Å)	c_{hex}/a_{hex}	V_{hex} (Å^3)	R_{wp}	R_B
$LiNi_{0.5}Co_{0.5}O_2$	2.84543 (3)	14.1311 (2)	4.9662	99.083 (2)	9.89	3.73
$LiNi_{0.45}Al_{0.05}Co_{0.5}O_2$	2.84217 (5)	14.1317 (6)	4.9722	98.862 (5)	10.00	3.75
$LiNi_{0.4}Al_{0.1}Co_{0.5}O_2$	2.83729 (7)	14.1378 (7)	4.9829	98.564 (6)	10.35	4.02
$LiNi_{0.35}Al_{0.15}Co_{0.5}O_2$	2.83356 (7)	14.1395 (8)	4.9900	98.318 (6)	10.20	4.25
$LiNi_{0.3}Al_{0.2}Co_{0.5}O_2$	2.82895 (8)	14.1405 (9)	4.9985	98.004 (7)	10.11	3.04
$LiNi_{0.25}Al_{0.25}Co_{0.5}O_2$	2.8257 (1)	14.142 (1)	5.005	97.788 (9)	10.15	2.61
$LiNi_{0.2}Al_{0.3}Co_{0.5}O_2$	2.8224 (1)	14.140 (1)	5.010	97.548 (9)	10.57	2.95

3.3. Morphological study (SEM)

Fig. 7a–d shows SEM micrographs of the $LiCo_{1-y}Al_yO_2$ and $LiNi_{0.5-y}Al_yCo_{0.5}O_2$ samples (y=0.0 and y=0.3) prepared in this work and calcined at 800 °C. The obtained powders consist of sub-micron particles, with a homogeneous size distribution. As it can be seen, in both $LiCo_{1-y}Al_yO_2$ and $LiNi_{0.5-y}Al_yCo_{0.5}O_2$ series, the substitution of either Co or Ni by Al results in small particle size, as was also observed by Myung et al. [16]for $LiCo_{1-y}Al_yO_2$ prepared by a different method, namely emulsion drying.

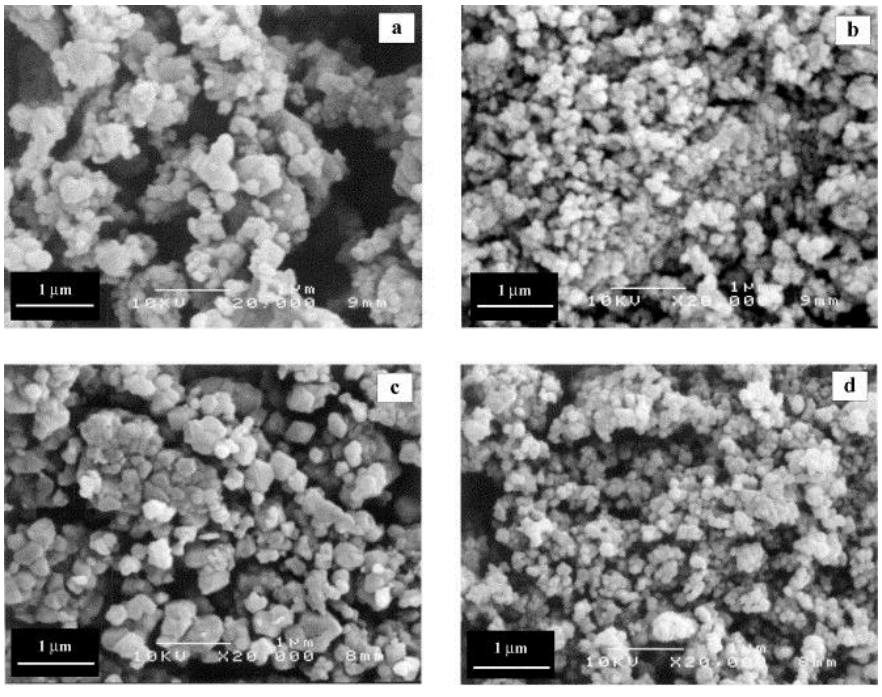

Fig. 7. SEM micrographs of (a) $LiCoO_2$, (b) $LiCo_{0.7}Al_{0.3}O_2$, (c) $LiNi_{0.5}Co_{0.5}O_2$ and (d) $LiNi_{0.2}Al_{0.3}Co_{0.5}O_2$ powders calcined at 800 °C.

Since smaller grain size can favor lithium ion penetration in the particles by reducing the ion diffusion pathway and therefore have a great influence on the electrochemical Li^+ intercalation and deintercalation processes, it is worth thinking about the factors that are limiting the kinetics of grain formation of these doped materials. We can speculate that the smaller particle size of the Al-doped materials is related to their wet-chemical synthesis assisted by carboxylic acid and the different coordinating characteristics of Al^{3+}ions compared to those of Ni^{2+} or Co^{2+}, which will in turn affect the distribution of the cations in the gel, the gel stability, the kinetics of its decomposition, etc. and, therefore, the particle characteristics. Further studies are needed to clarify this interesting point.

3.4. Local structure (FTIR)

FTIR spectroscopic studies provide additional information on the structure of the obtained oxides. The purpose of these studies is to investigate the local environment of the cations. Vibrational modes, which involve primarily atomic motion of cations against their oxygen neighbors, are sensitive to the crystal symmetry and cationic valence state and, consequently, frequency and strength of these modes are very sensitive to the cationic local environment in the host matrix [30].

$LiCo_{1-y}Al_yO_2$ and $LiNi_{0.5-y}Al_yCo_{0.5}O_2$ materials with layered structure and crystallographic $R\bar{3}m$ space group have a corresponding spectroscopic space group of D_{3d}^5. The factor group analysis yields four infrared-active modes ($2A_{2u}+2E_u$). Considering the structure built of MO_6 octahedra, the stretching modes of $(Co,Ni,Al)O_6$ octahedra occur in the high-frequency region (500–650 cm^{-1}), while the stretching mode of LiO_6 octahedra is observed in the far-infrared region around 250 cm^{-1} [30].

Fig. 8a and b shows the FTIR absorption spectra of the $LiCo_{1-y}Al_yO_2$ and $LiNi_{0.5-y}Al_yCo_{0.5}O_2$ samples, respectively. As expected, these spectra display several bands in the high-wavenumber region (at 400–650 cm^{-1}) corresponding to the broad rock-salt band, which is broken into several components, and the low-wavenumber band centered at 260 cm^{-1}, which expresses the Li–O vibrational modes.

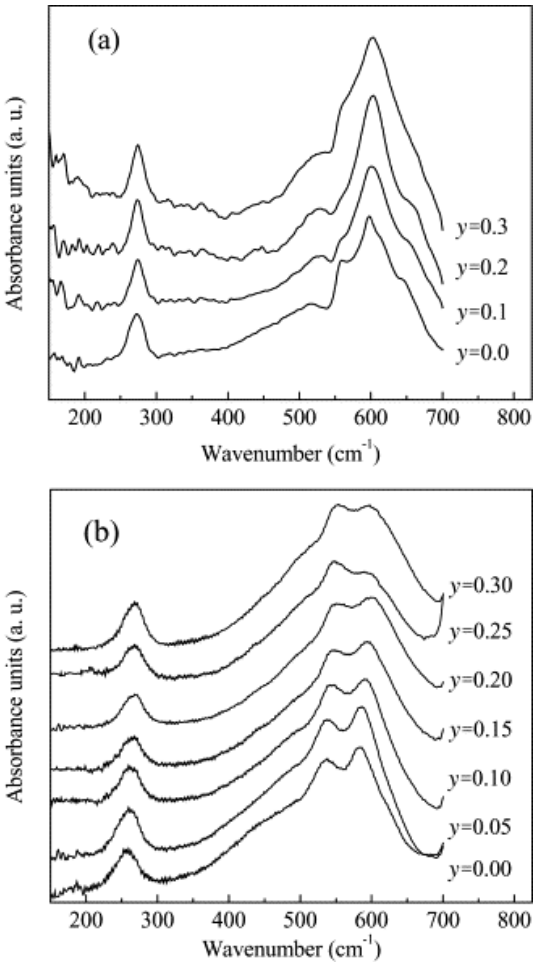

Fig. 8.
FTIR absorption spectra for (a) $LiCo_{1-y}Al_yO_2$ and (b) $LiNi_{0.5-y}Al_yCo_{0.5}O_2$ powders calcined at 800 °C.

Very interestingly, the regular variation of the infrared-bands position with aluminum content in $LiNi_{0.5-y}Al_yCo_{0.5}O_2$ oxides is indicating the formation of solid solutions where the two end-members display the same structure. Fig. 9a clearly shows the linear dependence of the M–O stretching modes (v_1 and v_2) upon Al substitution. Those M–O bands in the $LiNi_{0.5-y}Al_yCo_{0.5}O_2$ oxides are shifted to higher wavenumbers due to the incorporation of the smaller and lighter Al^{3+} ions in place of the larger and heavier Ni^{3+} ions. In the $LiCo_{1-y}Al_yO_2$ samples, the position of the two bands does not changed with aluminum content, while the two other bands are slightly shifted. This different behavior can be related to the smaller difference in the ionic size of Al^{3+} and Co^{3+} compared with Ni^{3+}.

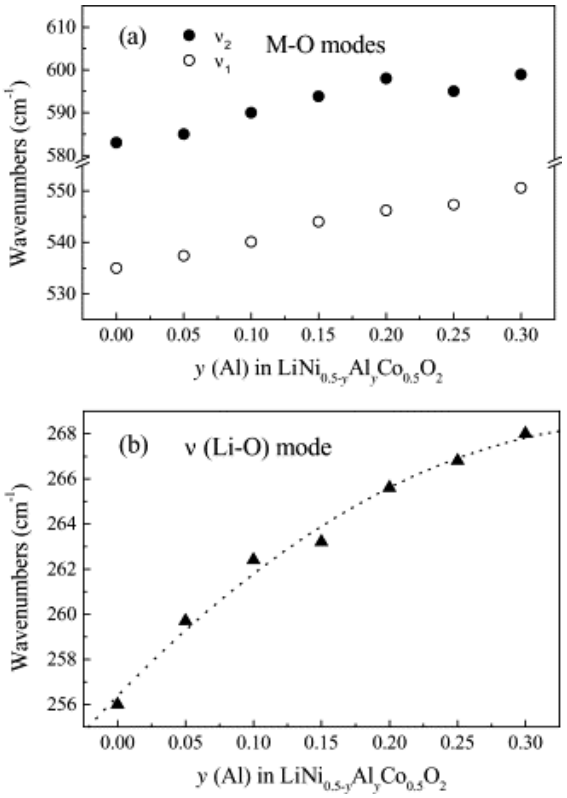

Fig. 9.
Compositional dependence of the wavenumber of the infrared modes of $LiNi_{0.5-y}Al_yCo_{0.5}O_2$ powders. (a) High-wavenumber bands (v_1 and v_2) attributed to M–O stretching modes and (b) low-wavenumber band (v_1) attributed to Li–O stretching mode.

As for the frequency variation of the Li–O band (v_3) with y, it does not occur to the same extent in the $LiCo_{1-y}Al_yO_2$ and $LiNi_{0.5-y}Al_yCo_{0.5}O_2$ materials: while the increase is clearly seen in the case of the Li–Ni–Al–Co samples, it is hardly noticeable in the Li–Co–Al materials. To understand this result, we have to look at how the Li–O distances change with y in both series, as deduced from the variation in the a_{hex} and c_{hex}parameters. As indicated above (Section 3.2), in the Li–Ni–Al–Co series, the predominant effect of the aluminum substitution on the cell parameters is the decrease in the a_{hex} parameter as y increases, with the concomitant shrinkage of the Li–O bond length (Fig. 9b). On the contrary, in the case of the $LiCo_{1-y}Al_yO_2$samples, both the decrease in the a_{hex} parameter and the increase in the c_{hex} parameter are important. As these variations have opposite effects on the Li–O bond length, in this series, this distance hardly changes with y and so does the frequency of the Li–O bands.

Therefore, FTIR measurements of the samples are consistent with the data obtained from X-ray powder diffraction.

3.5. Compositional analysis (ICP)

Elemental analysis realized by ICP show that the so-prepared $LiCo_{1-y}Al_yO_2$ and $LiNi_{0.5-y}Al_yCo_{0.5}O_2$ oxides ($0 \leq y \leq 0.3$) have a composition near the ideal one for all *y* values studied Table 3 and Table 4. These results prove that the wet-chemical synthesis assisted by succinic acid provides samples with the expected nominal composition, i.e. the metal composition ratio of the initially mixed materials is maintained during the synthesis and no significant loss of lithium oxide has occurred during the thermal treatment.

Table 3.
Elemental composition of $LiCo_{1-y}Al_yO_2$ ($0 \leq y \leq 0.3$) samples, obtained by ICP analysis

	Experimental composition (±0.01)		
Nominal composition	Li	Co	Al
$LiCoO_2$	1.04	0.96	–
$LiCo_{0.9}Al_{0.1}O_2$	1.05	0.86	0.09
$LiCo_{0.8}Al_{0.2}O_2$	1.10	0.71	0.19
$LiCo_{0.7}Al_{0.3}O_2$	1.04	0.68	0.28

Table 4.
Elemental composition of $LiNi_{0.5-y}Al_yCo_{0.5}O_2$ ($0 \leq y \leq 0.3$) samples, obtained by ICP analysis

	Experimental composition (±0.005)			
Nominal composition	Li	Ni	Al	Co
$LiNi_{0.5}Co_{0.5}O_2$	0.998	0.496	–	0.506
$LiNi_{0.45}Al_{0.05}Co_{0.5}O_2$	0.997	0.450	0.045	0.507
$LiNi_{0.4}Al_{0.1}Co_{0.5}O_2$	1.000	0.397	0.097	0.506
$LiNi_{0.35}Al_{0.15}Co_{0.5}O_2$	0.996	0.347	0.147	0.510
$LiNi_{0.3}Al_{0.2}Co_{0.5}O_2$	1.001	0.297	0.194	0.507
$LiNi_{0.25}Al_{0.25}Co_{0.5}O_2$	0.986	0.253	0.244	0.517
$LiNi_{0.2}Al_{0.3}Co_{0.5}O_2$	0.980	0.203	0.296	0.521

3.6. Electrochemical study

Fig. 10 shows the charge–discharge profiles of Li□$LiNi_{0.5-y}Al_yCo_{0.5}O_2$ ($0.0 \le y \le 0.3$) cells using positive electrode materials prepared by the sol–gel method.

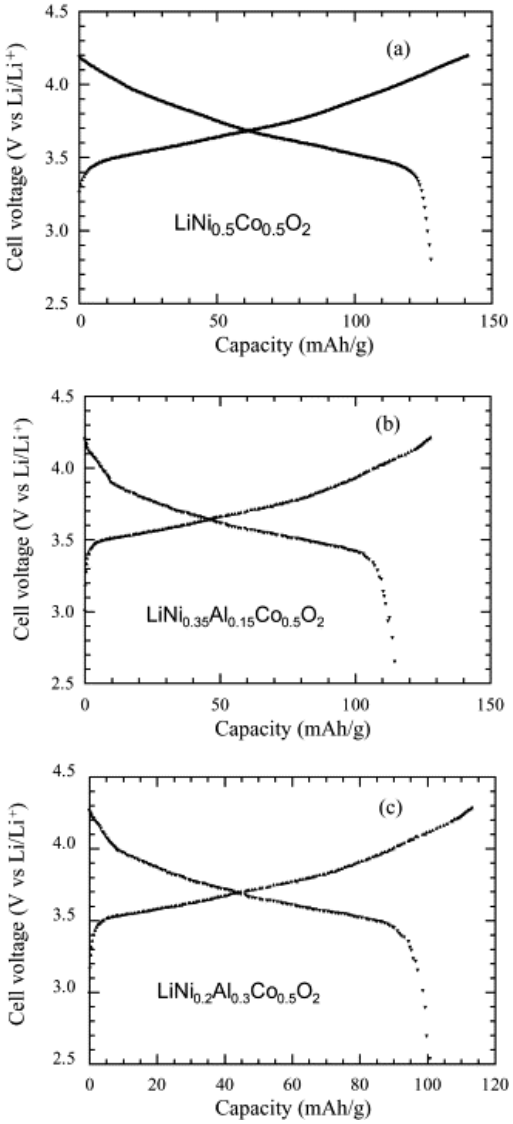

Fig. 10. Electrochemical features of Li□$LiNi_{0.5-y}Al_yCo_{0.5}O_2$ cells during the first charge–discharge cycle: (a) y=0.00, (b) y=0.15 and (c)y=0.30.

The first general observation is that in the potential domain 2.5–4.2 V, the charge–discharge curves approximately correspond to the voltage profiles characteristic of the $LiCoO_2$ electrode materials associated with lithium occupation of octahedral sites, in agreement with the general trends observed for lithium cobaltates [1], [2] and [3]. However, these data also confirm previous results, which have acknowledged that low-temperature synthesized $Li_xCo_{1-y}Ni_yO_2$ cathode materials exhibit a lower potential for lithium intercalation–deintercalation than the materials prepared at high temperature by a solid state reaction [31]. Also, they show that in the Al-doped materials, the wide plateau observed in the charge–discharge curves of $LiCoO_2$ at ca. 3.7 V

disappears (Fig. 10). This is mainly due to the presence of Ni^{3+}ions, which are preferentially oxidized to Ni^{4+} before cobalt in Ni-substituted compounds [32]. Thus, at low degree of Li extraction, the electrochemical features resemble those of Li_xNiO_2 with a stabilization of the 2D framework. Consequently, the charge–discharge profiles have a $LiNiO_2$-like character without the disadvantages of the multiple-phase system exhibited by this compound [2].

The slight variation of the average potential with Al substitution for Ni is also observed in Fig. 10. This effect is primarily attributed to the change in the electronic structure of $LiNi_{0.5-y}Al_yCo_{0.5}O_2$ compounds on addition of Al ions and, thus, in the small variation in the Fermi level [26]. It should be also remarked that the fully intercalated phase is not recovered during the first discharge. The capacity retention could be probably assigned to a kinetic problem especially as the phase $LiNi_{0.5-y}Al_yCo_{0.5}O_2$ is a poor electronic conductor. Recent reports have also stated that passivation of the positive electrode could appear during the first charge–discharge process [33]. However, the polarization during both charge and discharge is almost similar in all cells.

The shape of the charge–discharge curves shows good reversibility and capacity retention during the first cycle for all studied $LiNi_{0.5-y}Al_yCo_{0.5}O_2$ compounds. These studies demonstrate that cathodes yield capacities around 115 mA h/g for $LiNi_{0.35}Al_{0.15}Co_{0.5}O_2$ when discharged to a cut-off voltage of 2.5 V. There is ~15% loss of capacity for a single charge and discharge cycle to 4.2 V in the $LiNi_{0.2}Al_{0.3}Co_{0.5}O_2$ oxide. The steady variation in cell potential, as Li ions are extracted, indicates that, in the Li concentration range explored for this compound, the material appears to be single phase. In the composition domain $0.4 \le x \le 1.0$, the voltage charge profile of the Li□$Li_xNi_{0.5-y}Al_yCo_{0.5}O_2$ cells exhibits a continuous increase of the potential without formation of a voltage plateau. For $x<0.5$, the high-voltage limit (4.2 V) imposed in the experiments is rapidly reached. However, the cell potential of the Al-substituted electrodes is generally higher than the undoped $LiCoO_2$ positive electrode, which is consistent with theoretical predictions and experiments on powder samples [34].

The high insertion capability has been confirmed by measuring the chemical diffusion coefficients of Li ions in the structure, as shown in Fig. 11a and b. D_{Li^+} has been investigated in the compositional range $0.5 \le x \le 1.0$ corresponding to the single-phase region. The measured values of D_{Li^+} for $Li_xNi_{0.5-y}Al_yCo_{0.5}O_2$powders are in the range 5×10^{-10} to 4×10^{-9} cm^2/s in the Li concentration interval explored corresponding to the voltage range 2.5–4.2 V vs. Li/Li^+.

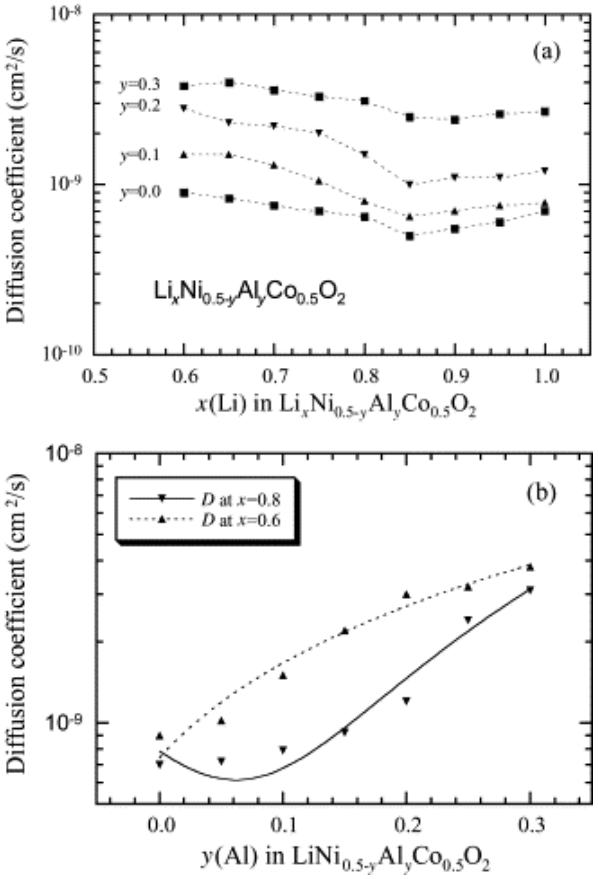

Fig. 11.
Chemical diffusion coefficients (D_{Li}^+) of Li^+ ions in LixNi$_{0.5-y}$AlyCo$_{0.5}$O$_2$ powders calcined at 800 °C. (a) Plots of D_{Li}^+ as a function of (x)Li content. (b) Plots of D_{Li}^+ as a function of y(Al) concentration for x(Li)=0.8 and 0.6.

For a given Al content, the general trend as the Li content diminishes is a slight decrease of the D_{Li}^+ values in the range $1.0 \geq x \geq 0.85$, while for Li concentration less than 0.8, these D_{Li}^+ values increase again (Fig. 11a). Also, the D_{Li}^+ for the discharge reaction is slightly greater than that of the charge process. This variation in the values of D_{Li}^+ with the Li content can be explained referring to the crystal structure of those LixNi$_{0.5-y}$AlyCo$_{0.5}$O$_2$ materials and taking into account the factors that influence the intercalation process, namely: (i) the number of mobile ions; (ii) the degree of ion occupancies; (iii) the degree of covalency of Li–O bonds; (iv) the separation between [MO_2] layers or the size of the pathways for the Li ions. In this context, the higher the number of mobile species, the lower the number of ions that impede their movement, the larger their diffusion paths and the lower the covalency of the Li–O bonds, the more favored diffusion will be[35]. In our case (Fig. 11a), the initial decrease of D_{Li}^+ as x decreases would be due to the diminution in the number of Li^+ ions in the material while the increase in D_{Li}^+ for lower x content would be probable by the opening of larger diffusion paths in the structure as more Li^+ ions are removed from the interslab space.

On the other hand, aluminum substitution also provides an increase of chemical diffusion coefficients of Li ions in the $Li_xNi_{0.5-y}Al_yCo_{0.5}O_2$ lattice: as it can be seen in Fig. 11a and b, for a given x, D_{Li}^+ can increase nearly one order of magnitude with y (aluminum content). In this case, substitution of Al^{3+} for Ni^{3+} enlarges the c-axis crystallographic parameter due to an increase in the separation between $[MO_2]$ layers, which in turn favors the diffusion of Li^+ ions as it take place through larger pathways.

The measured values are of the order of the chemical diffusion coefficients reported for other lithium cobaltates: D_{Li}^+ was stated to be between 9×10^{-9} and 5×10^{-8} cm^2/s for $0.1\leq x\leq1.0$ in Li_xCoO_2 [36] and [37], and of 2.5×10^{-10} cm^2/s in $Li_{0.5}CoO_2$ [38]. According the relationship $D_{Li}^+=L^2/\tau$, where L is the radius of the crystal grain and τ is the characteristic time for Li^+ diffusion, an average value of 10^{-9} cm^2/s for D_{Li}^+ in $Li_xNi_{0.5-y}Al_yCo_{0.5}O_2$ powders means that the size of the particles has to be ≤0.8 μm in order to be fully discharged in 60 s or less. This drastic condition is well fulfilled in our $LiNi_{0.5-y}Al_yCo_{0.5}O_2$ powders.

4. Conclusions

$LiCo_{1-y}Al_yO_2$ and $LiNi_{0.5-y}Al_yCo_{0.5}O_2$ ($0\leq y\leq0.3$) solid solutions have been synthesized by a sol–gel method using succinic acid as chelating agent. X-ray diffraction patterns show that all the samples are single phase and have the layered α-$NaFeO_2$ structure. The regular variation of the lattice parameters and the IR frequency modes indicate the formation of the solid solutions. Aluminum doping increases the interval of thermal stability favoring the formation of well-crystallized $LiCo_{1-y}Al_yO_2$ and $LiNi_{0.5-y}Al_yCo_{0.5}O_2$ powders at lower temperatures and preventing the loss of lithium from the structure. The grain size decreases upon doping and this fact can favor the lithium diffusion. Both the initial charge and discharge capacities decrease as the aluminum content gets higher. However, more stable charge–discharge cycling performances have been obtained as compared to those displayed by the native oxides. Li ion diffusion coefficients increase with Al^{3+} doping due to the increase in the interlayer distance and the decrease of the size of the particles; these results are in agreement with XRD, FTIR and SEM data.

Acknowledgements

The authors wish to thank the Spanish and the French Foreing Office (HF 1999-0101, PAI Picasso 00717TC) and the University of A Coruña for financial support.

References

1. T. Ohzuku
   Lithium Batteries, New Materials, Developments and Perspectives, Elsevier, Amsterdam (1993), p. 239

2. C. Delmas, I. Saadoune
   Solid State Ionics, 53–56 (1992), p. 370

3. T. Ohzuku, A. Ueda, M. Nagayama, Y. Iwakoshi, H. Komori
   Electrochim. Acta, 38 (1993), p. 1159

4. C.D.W. Jones, E. Rosen, J.R. Dahn
   Solid State Ionics, 68 (1994), p. 65

5. R. Stoyanova, E. Zhecheva, L. Zarkova
   Solid State Ionics, 73 (1994), p. 233

6. W. Huang, R. Frech
   Solid State Ionics, 86–88 (1996), p. 395

7. G.A. Nazri, A. Rougier, K.F. Kia
   Mater. Res. Soc. Symp. Proc., 453 (1997), p. 635

8. R. Alcantara, P. Lavela, J.L. Tirado, R. Stoyanova, E. Zhecheva
   J. Solid State Chem., 137 (1997), p. 265

9. H. Tukamoto, A.R. West
   J. Electrochem. Soc., 144 (9) (1997), p. 3164

10. I. Saadoune, C. Delmas
    J. Solid State Chem., 136 (1998), p. 8

11. C. Julien, M.A. Camacho-López, T. Mohan, S. Chitra, P. Kalyani, S. Gopukumar
    Solid State Ionics, 135 (2000), p. 241

12. M. Mladenov, R. Stoyanova, E. Zhecheva, S. Vassilev
    Electrochem. Commun., 3 (2001), p. 410

13. A. Choblet, H.C. Shiao, H.P. Lin, M. Salomon, V. Manivannan
    Electrochem. Solid-State Lett., 4 (6) (2001), p. A65

14. R.D. Shannon
    Acta Crystallogr., A32 (1976), p. 751

15. R. Alcantara, P. Lavela, P.L. Relaño, J.L. Tirado, E. Zhecheva, R. Stoyanova
Inorg. Chem., 37 (1998), p. 264

16. S.T. Myung, N. Kumagai, S. Komaba, H.T. Chung
Solid State Ionics, 139 (2001), p. 47

17. W.S. Yoon, K.K. Lee, K.W. Kim
J. Electrochem. Soc., 147 (6) (2000), p. 2023

18. Y.I. Jang, B. Huang, H. Wang, D.R. Sadoway, G. Ceder, Y.M. Chiang, H. Liu, H. Tamura
J. Electrochem. Soc., 146 (3) (1999), p. 862

19. G. Ceder, Y.M. Chiang, D.R. Sadoway, D.R. Aydinol, Y.I. Jang, B. Huang
Nature, 392 (1998), p. 694

20. C. Delmas, M. Menetrier, L. Croguennec, I. Saadoune, A. Rougier, C. Pouillerie, G. Prado, M. Grune, L. Fournes
Electrochim. Acta, 45 (1999), p. 243

21. G.X. Wang, S. Zhong, D.H. Bradhurst, S.X. Dou, H.K. Liu
Solid State Ionics, 116 (1999), p. 271

22. T. Ohzuku, T. Yanagawa, M. Kouguchi, A. Ueda
J. Power Sources, 68 (1997), p. 131

23. C.N.R. Rao
J. Mater. Chem., 9 (1999), p. 1

24. C.J. Howard, B.A. Hunter, Rietica: A Computer Program for Rietveld Analysis of X-Ray and Neutron Powder Diffraction Patterns, Australian Nuclear Science and Technology Organization, Lucas Heights Research Laboratories (February 1997).

25. W. Weppner, R.A. Huggins
J. Electrochem. Soc., 124 (1977), p. 1569

26. S. Castro-Garcia, C. Julien, M.A. Señaris-Rodriguez
Int. J. Inorg. Mater., 3 (2001), p. 323

27. A. Rougier, I. Saadoune, P. Gravereau, C. Delmas
Solid State Ionics, 90 (1996), p. 83

28. A. Rougier, P. Gravereau, C. Delmas
J. Electrochem. Soc., 143 (1996), p. 1168

29. J.R. Dahn, U. von Sacken, C.A. Michael
Solid State Ionics, 44 (1990), p. 87

30. C. Julien
Solid State Ionics, 136–137 (2000), p. 887

31. C. Julien, G.A. Nazri
Mater. Res. Soc. Symp. Proc., 548 (1999), p. 79

32. D. Caurant, N. Baffier, B. Garcia, J.P. Pereira-Ramos
Solid State Ionics, 91 (1996), p. 45

33. A. Le Gal La Salle, A. Verbaere, Y. Piffard, D. Guyomard
C. Julien, Z. Stoynov (Eds.), Materials for Lithium-Ion Batteries, Kluwer Academic Publishing, Dordrecht (2000), p. 241

34. Y.I. Jang, B. Huang, H. Wang, Y.M. Chiang, D.R. Sadoway
Mat. Res. Soc. Symp. Proc., 496 (1998), p. 403

35. B. Yebka, C. Julien
Solid State Ionics, 90 (1996), p. 141

36. A. Honders, J.M. der Kinderen, A.H. van Heeren, J.H.W. de Wit, G.H.J. Broers
Solid State Ionics, 15 (1985), p. 265

37. M.G.S.R. Thomas, P.G. Bruce, J.B. Goodenough
Solid State Ionics, 17 (1985), p. 13

38. Y.I. Jang, B.J. Neudecker, N.J. Dudney
Electrochem. Solid-State Lett., 4 (2001), p. A74

Corresponding author. Tel.: +34-981-16-70-00; fax: +34-981-16-70-65